Research Article | Vol. 13, No. 1 / 1 Jan 2023 / Optical Materials Express 119
Optical Materials EXPRESS

Auger electron spectroscopy mapping of lithium niobate ferroelectric domains with nano-scale resolution

TORREY MCLOUGHLIN,[1,*] WM. RANDALL BABBITT,[1] AND WATARU NAKAGAWA[2]

[1]Department of Physics, Montana State University, Bozeman, Montana 59717-3840, USA
[2]Electrical & Computer Engineering Department, Montana State University, Bozeman, Montana 59717-3780, USA
[*]torrey.mcloughlin@montana.edu

Abstract: The +/−Z ferroelectric domains in periodically poled lithium niobate are characterized with Auger electron spectroscopy. The -Z domains have a higher Auger O-KLL transition amplitude than the +Z domains. Based on this, Auger electron spectroscopy mapping can be used on the O-KLL peak to image the +/-Z domain structure. This new characterization technique is confirmed with HF etching, and compared to SEM imaging. Spatial resolution down to 68 nm is demonstrated.

1. Introduction

In order to support the large scale fabrication of nano-scale poled domains in lithium niobate, a suitable characterization method is required. Despite the advances in this field, the available characterization methods have individual deficiencies. Long scan times, probe contact-degradation [1], complicated or unknown mechanisms of image contrast [2–4], domain ambiguity [5–8], destruction of the crystal surface [9,10], and limited resolution due to optical diffraction [11,12], probe-tip size [1,13,14], and sample charging [15–17] are all potential drawbacks. A new characterization method that complements the existing techniques would be useful if it could facilitate this domain characterization.

Auger electron spectroscopy (AES) has previously been demonstrated as a tool for domain differentiation on un-etched PPLN samples, due to the separation in peak amplitude of the Auger O-KLL peak between +/-Z domains [18]. Based on this principle, AES elemental mapping is adapted to image +/-Z domains in periodically poled lithium niobate. AES mapping is an imaging method where each pixel's value represents the AES amplitude at a specified energy. AES mapping is generally used to characterize the presence of elements and their density in a sample but is adapted here to determine +/-Z ferroelectric domain orientations unambiguously in periodically poled lithium niobate (PPLN). AES mapping is non-destructive, as it requires no mechanical surface contact. The results are compared with SEM images and confirmed with the results from HF etching of the sample. Finally, nano-scale resolution is demonstrated down to an apparent domain wall width of approximately 68 nm, though higher resolution is likely possible.

2. Experiment

AES maps of ferroelectric domains in PPLN are produced using a PHI 710 Auger Nanoprobe. The Z-cut, double-side polished, congruent PPLN wafer was obtained from G&H and has a 15 μm poling period with an assumed duty cycle of 50% (+/-Z domains are the same width). The wafer was coated with photoresist to protect it and was then diced into 10 mm × 10 mm chips. The chips were subsequently cleaned in a sonicated acetone bath, rinsed with isopropyl alcohol, then DI water, and dried. The PPLN samples are tilted to 75° relative to the axis of

#474717 https://doi.org/10.1364/OME.474717
Journal © 2023 Received 2 Sep 2022; revised 11 Nov 2022; accepted 4 Dec 2022; published 13 Dec 2022

Optical Materials EXPRESS

the electron beam and the cylindrical mirror analyzer. Tilting the samples is necessary in order to prevent the insulating lithium niobate (LN) from charging by matching the escape depth of emitted electrons to the probe depth of incident primary electrons [19,20]. Oxygen's Auger KLL transition (nominally at 531 eV [21]) is found to be the most prominent peak in the LN AES spectrum, and is used for this analysis. The rest of the loading process and system setup is described in a previous work [22].

Mapping on LN is acquired in the following way. First, the region of interest is focused using the SEM. An AES spectrum is next taken that covers an energy range generally at least 30 eV below and above the nominal peak position due to the O-KLL transition energy typically being shifted by sample charging. Once the current O-KLL peak energy is determined, a map is taken with the mapping energy chosen on the high side of the O-KLL energy peak position, due to the peak's tendency to drift to higher energy due to charging. Consecutive maps are taken at relatively low-resolution, stepping down in energy from above the O-KLL transition energy until domain contrast appears. The optimal mapping energy is determined based on best contrast, at which point the mapping resolution and dwell time per pixel are increased as needed. If domain contrast decreases during map acquisition, it is likely due to a drift in the O-KLL peak energy, which can occur if the field of view (FOV) is too large, or primary beam current too low. Counterintuitively, decreasing the FOV or increasing the beam energy/current, although it is increasing the incident charge density, tends to stabilize the O-KLL peak's energy. Conversely, if the FOV is too low or current too high, sample charging will cause the FOV to drift, and thus the FOV and the beam current must be balanced to some extent. The mapping results presented here were taken with primary beam voltage of 5 kV, beam currents of 5 nA or 10 nA, and FOVs of 50 μm, 20 μm, and 9 μm.

3. Results

Figure 1(a) is a 20 μm FOV SEM image of the PPLN sample with a 15 μm period. Figures 1(b)–(d) are single point AES maps of the same region with varying parameters. The AES map in Fig. 1(b) was taken at 520 eV and shows the domain contrast is low when the mapping energy is too far off of the peak. Figure 1(c) is an AES map at 510 eV where the domain contrast is visible. Both Figs. 1(b) and 1(c) were 256 × 256 pixels, and taken with an integration time of 1.0 ms/pixel. Figure 1(d) is a higher resolution AES map taken at 510 eV with 1024 × 1024 pixels, giving a pixel-to-pixel distance of 19nm, and an integration time of 5.0 ms/pixel. All four panels in Fig. 1 were taken with a 5 kV, 5 nA primary beam. In the AES maps, -Z domains are brighter than the +Z domains, allowing immediate determination of domain polarity. Notably, previous methods of domain differentiation using AES did not allow full domain imaging, and required acquisition of a full O-KLL spectrum for each spatially averaged survey area as well as significant post-processing in order to perform precise peak-fitting for comparison [18,22]. The AES mapping technique demonstrated here (e.g. in Fig. 1(d)) requires the signal at only a single energy, and each pixel correlates to a single beam spot rather than an averaged survey area. In the SEM image, the domain walls (DW) can be located, but unambiguously determining the domain polarization is not possible due to the inconsistent brightness, where one -Z domain has both brighter and darker regions than the +Z domains. This issue has been discussed in the literature, with varying theories on which domain is brighter and whether the contrast changes or reverses under beam exposure and certain beam parameters [6,7,23]. As noted, the sample is tilted 75 degrees in Fig. 1, such that the vertical direction in the images covers a distance of 77 μm on the sample surface.

Image processing is performed in order to enhance the domain differentiation. First, a group of bad pixels along the edge of the image with values of zero (27 total pixels) are set to the average pixel value. In order to remove the horizontal scanning artifacts of the AES, each row is normalized by the mean value of the row. Next, because the pixel-to-pixel noise is generally

Optical Materials EXPRESS

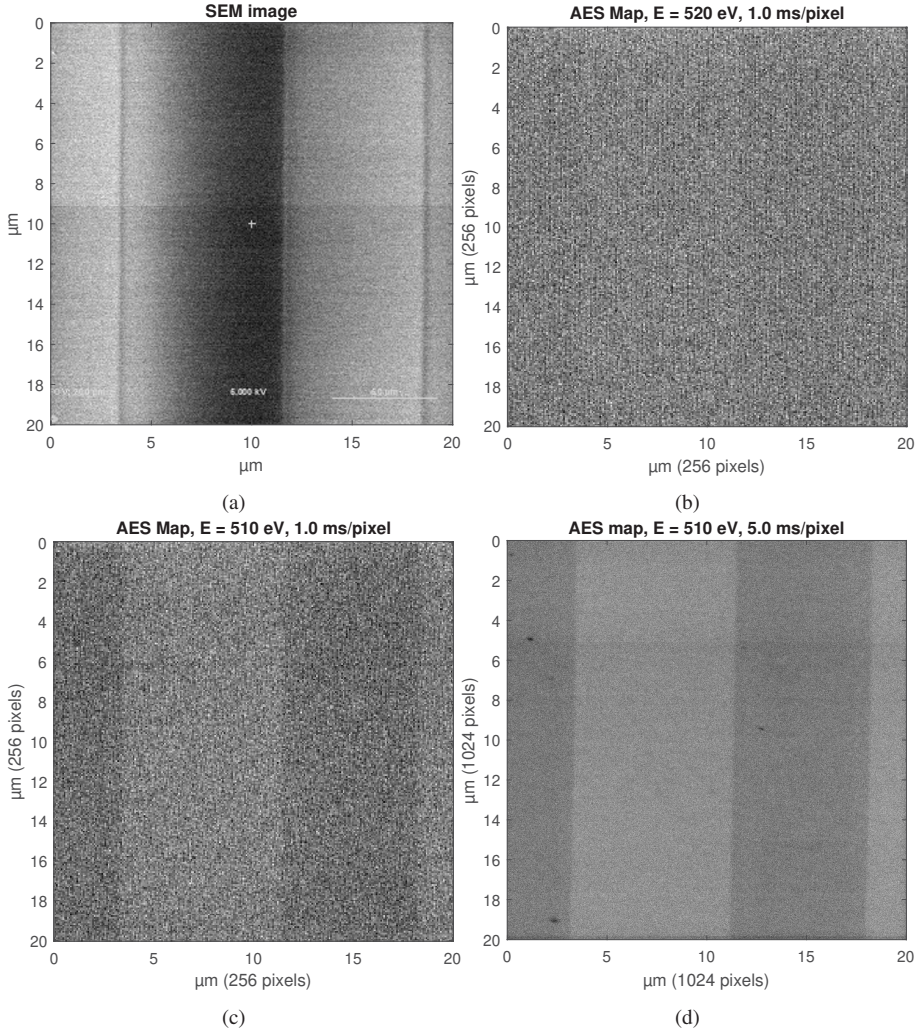

Fig. 1. (a) SEM image and (b)–(d) AES maps of the same PPLN region with different parameters: (b) AES Map at 520 eV, above the O-KLL peak, where domain contrast is low; (c) AES Map at the optimal energy, 510 eV, with 256×256 pixels and 1.0 ms/pixel dwell time; (d) AES map at 510 eV with higher resolution, 1024× 1024 pixels, and 5.0 ms/pixel dwell time. Gray-scale range limits (black/white) in (b)–(d) set to the min/max of each image.

Optical Materials EXPRESS

larger than the signal separation between domains, Gaussian smoothing is applied. The standard deviation of the smoothing (σ) is chosen as the value that allows the walls to be readily identified as peaks in a differentiated lineplot. An AES map smoothed with σ = 7 is shown in Fig. 2(a), where the process is applied to the AES map from Fig. 1(d). Figure 2(b) shows the lineplots for all of the rows of pixels from Fig. 2(a). The lineplots are stratified into two levels due to the smoothing, and the three horizontal lines are the chosen upper/lower thresholds, and the mean value (1 due to normalization). The upper and lower thresholds were chosen to optimize the certainty in identification of the poling domain orientation. While this image processing results in a poorer spatial resolution, it likely does not affect the precision of the AES mapping method's ability to determine the domain wall's location. Figure 2(c) is a thresholded image of the AES map after smoothing, where gray, black, and green pixels correspond to above the upper threshold, below the lower threshold, and in between the two, respectively. The green pixels represent the uncertain location of the DWs between the two thresholds. The apparent DW width in pixels is determined by observing the number of green pixels in a row and dividing by the number of DWs. The apparent DW width averaged over all the rows in this image is 6.25 pixels or 122 nm. We also calculate from this image a period of 14.97 μm and a duty cycle (+Z domain width divided by the period) of 0.454. For comparison with another characterization method, the SEM image from Fig. 1(a) has the same image processing applied to it in Fig. 2(d), and the green pixels from Fig. 2(c) are overlaid on the image. Comparing the observed position of the DWs in the SEM image (grayscale) with the AES mapping results (green overlay), the DWs appear to coincide within approximately one linwidth.

Another region of the sample analyzed above is shown in Fig. 3, where the domain widths vary slightly as a function of position producing "wavy" domain edges. Figure 3(a) is the Auger Nanoprobe's SEM image. Note the brightness change across the image such that +/-Z domains cannot be unambiguously determined. Figure 3(b) is the AES map of the same region. Note the consistent bright/dark contrast between domains, as well as the horizontal lines due to the left-to-right scanning. Figure 3(c) is the thresholded image from the AES map in 3(b), after line-by-line normalization to remove the horizontal scanning artifacts, and Gaussian smoothing with σ = 6. This region with wavy domain edges was chosen in order to show AES mapping's ability to characterize ambiguous regions with non-uniform DWs. It is important to note that the line-by-line normalization used to remove scanning artifacts relies on the fact that the region contains roughly equal amounts of both +/-Z domain in each horizontal row of pixels. For non-periodic structures or other situations where this assumption is invalid, a different normalization process would be needed.

One particularly important aspect of AES mapping is that +Z domain orientation can be characterized unambiguously since the -Z domains have a consistently higher Auger O-KLL signal amplitude. This can be compared with SEM images, where the +/-Z domain contrast is not always consistent. In order to confirm that the domain orientation measured using AES mapping is correct, we also performed an HF etch on the sample. Since HF is known to preferentially etch the -Z domains [24–30], analysis of the sample after etching confirms the size, shape and location of the poling domains. The HF etch method shows the domain orientation in the sample, but the etch process alters the sample and is not reversible. The SEM images (taken using a Zeiss SUPRA 55VP) in Fig. 4(a)–(b) show the sample prior to HF etch, where (a) is an in-lens detector image, and (b) is an SE2 detector image. In both cases, the domain orientation cannot be conclusively determined from the image. After HF etch, an image of the sample taken using the SE2 detector is shown in Fig. 4(c). The surface relief observed in the image indicates the domain orientation, with the +Z domains appearing in relief as they are not etched by HF. The results obtained using HF etch and SEM imaging are compared with the AES mapping approach in Fig. 4(d). Here, the SEM image after HF etch is overlaid with the domain edges identified using AES mapping in Fig. 3(c). The SEM image is rotated 2 degrees and the AES map's green pixels

Optical Materials EXPRESS

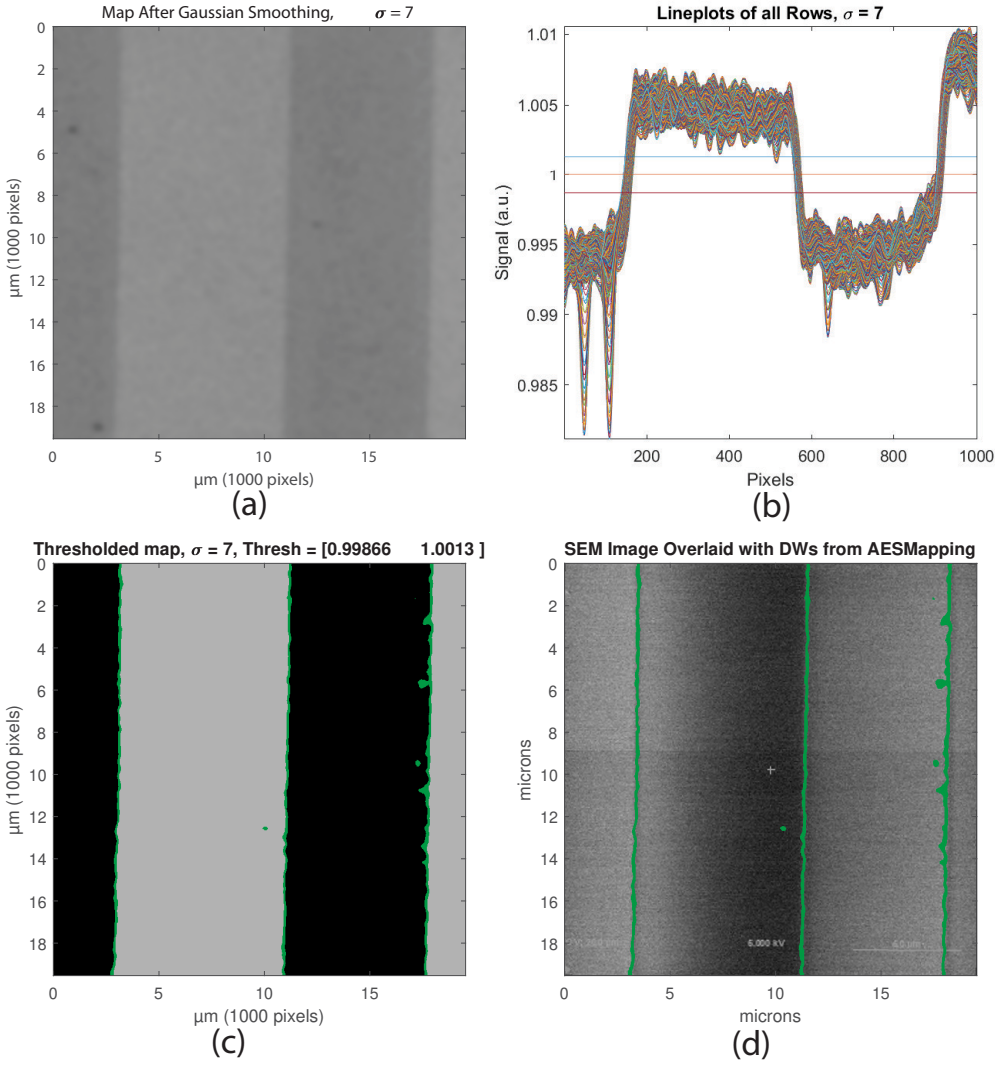

Fig. 2. (a) AES mapping image of PPLN (from Fig. 1(d)) after Gaussian smoothing with $\sigma = 7$, and line-by-line normalization. (b) Lineplots of all data rows from (a), showing separation into two levels after smoothing. The blue, red and purple lines indicate the upper threshold, average value, and lower thresholds, respectively. (c) Thresholded image, with grey, black, and green pixels corresponding to above the upper threshold, below the lower threshold, and in between the two, respectively. (d) Gaussian smoothing and line-by-line normalization used in (a) applied to corresponding SEM image, with the green pixels from (c) overlaid in order to compare the two methods. In all the images, the 75° tilt of the sample means the vertical range covers a projected distance of 77 µm on the sample surface.

Optical Materials EXPRESS

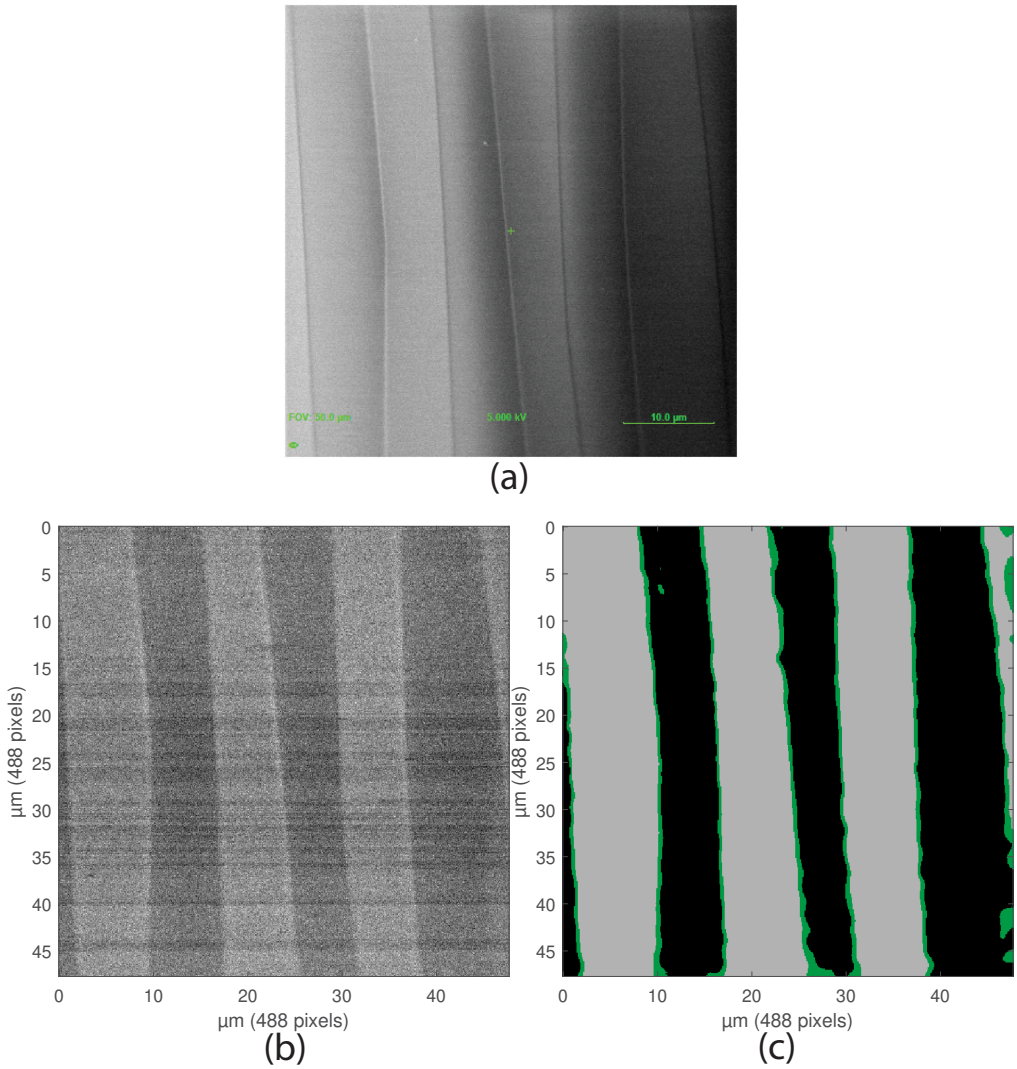

Fig. 3. (a) SEM image taken in a different area of the sample shown above, where the domain walls are not straight. (b) AES map at 515 eV of the same region as the SEM image, with 1.0 ms/pixel dwell time, and a primary beam voltage of 5 kV, and primary beam current of 5 nA. (c) Thresholded image from (b), where gray pixels are above the upper threshold, black pixels are below the lower threshold, and green pixels are in between the two.

Optical Materials EXPRESS

are translated 13 pixels in order align the two images. The -Z domains found in the AES map are slightly wider than their HF etched counterparts, a discrepancy in need of further exploration. However, the domains identified using these two methods generally agree, indicating that for this example, the AES mapping technique is able to unambiguously determine the domain orientation in a periodically poled sample, even with slightly wavy domain walls.

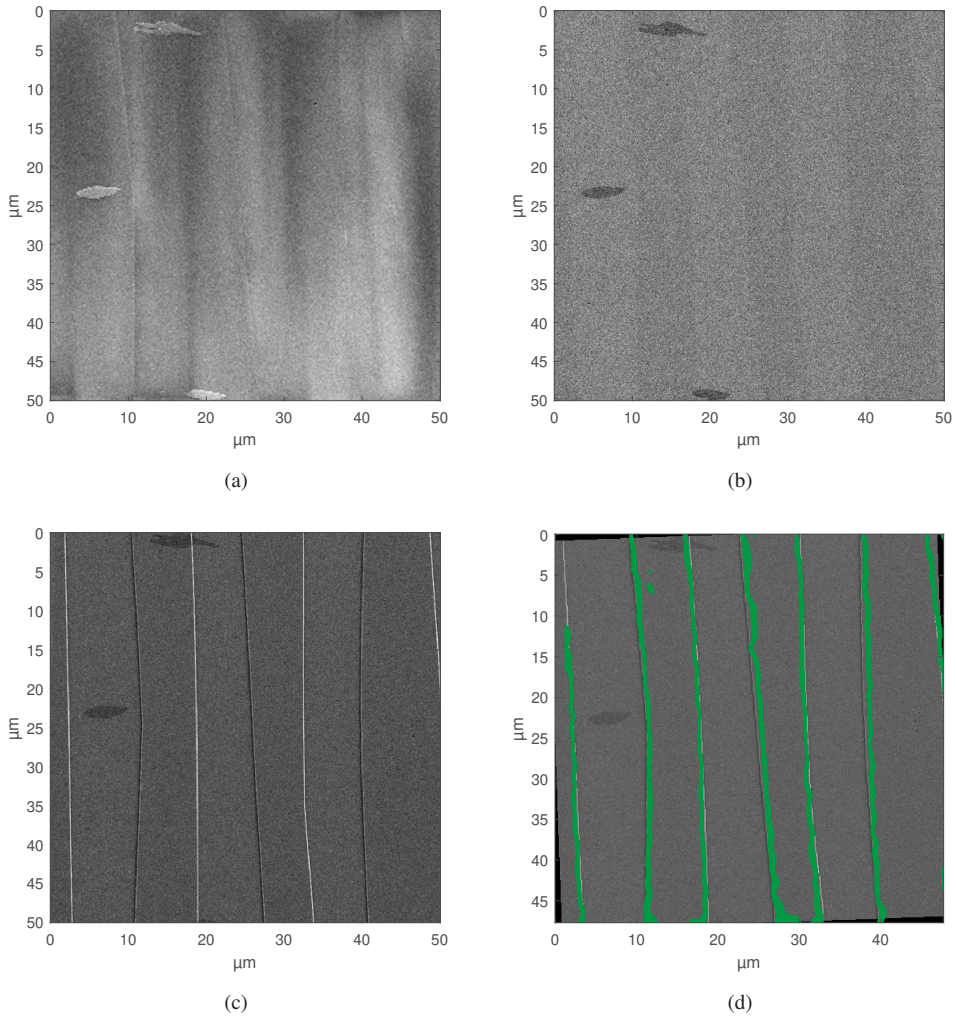

Fig. 4. SEM images of the same region from Fig. 3 taken with (a) in-lens detector, (b) SE2 detector, and (c) SE2 detector after HF etching the sample, confirming the etched -Z domains are the brighter regions in the AES maps. (d) The same SE2 image as (c) with the domain walls (green pixels) found in Fig. 3(c) overlaid on the image.

An important aspect of any characterization method for ferroelectric domains is spatial resolution. Perhaps the most relevant limitation to AES mapping is the potential for sample charging and the need to balance image drift with O-KLL peak energy drift. Figure 5 is an AES map with a relatively small, 9 µm FOV. The map was taken at 505 eV, 5 kV, 10 nA primary beam, and 512 × 512 pixels at 5 ms/pixel. The pixel-to-pixel distance is less than 18 nm. The AES map is processed as described above with a Gaussian smoothing standard deviation of $\sigma = 2$. In the thresholded image in Fig. 5(b), the average number of green pixels traversing the DW is just 3.85

Optical Materials EXPRESS

pixels. This corresponds to a spatial dimension of 67.7 nm. This is very likely larger than the actual DW width, expected to be on the scale of a single or few lattices wide [31,32]. However, there is also room to improve the nano-scale resolution demonstrated in Fig. 5, either by using a larger number of pixels, a lower FOV if it can be balanced against the image drift, or higher beam current to improve the signal to noise, as well as improved image processing in order to limit the required smoothing. Although a spatial resolution of 67.7 nm cannot yet measure the domain wall width directly, the demonstrated non-contact, surface ferroelectric domain imaging method using AES mapping, with a range of FOVs from single to hundreds of microns, is an important complementary tool to existing characterization methods.

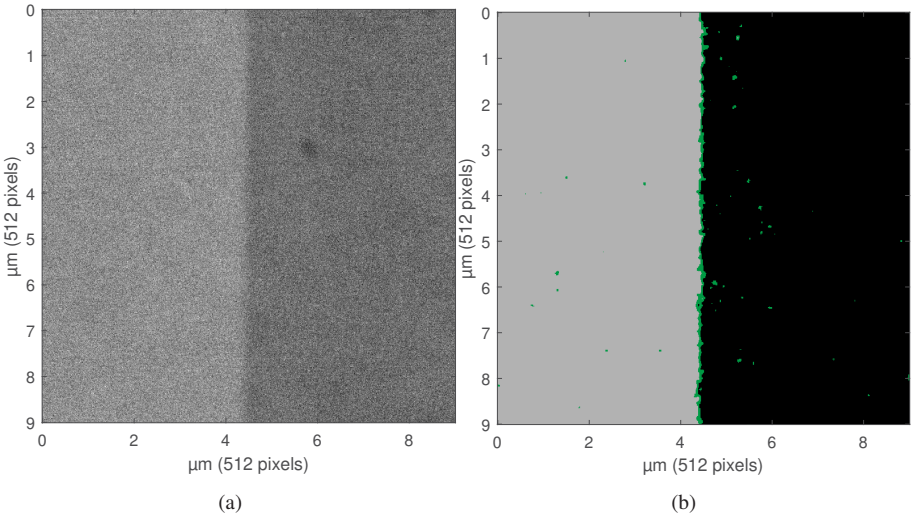

Fig. 5. (a) AES map with a 9 µm FOV showing just one domain wall. (b) Thresholded image, where green pixels represent values between the upper and lower thresholds. The average number of pixels across the domain wall is 3.85 pixels, giving an apparent domain wall width of 67.7 nm.

4. Discussion

It is important to note the current limitations of AES mapping. Due to the sample tilt of 75°, when the center of the image is in focus, the top and bottom edges of the images are out of focus and this effect is worse for larger FOVs. Despite this limitation, it is worth noting that the Auger mapping method demonstrated here allows both sub-micron resolution as well as FOVs of 100's of microns, a large dynamic range when compared with the dynamic range of FOVs of similar unambiguous surface characterization methods, such as PFM. Charging is an issue and as noted above, it can cause the O-KLL peak energy to drift, or the image FOV to drift. Better methods of charge mitigation would improve spatial resolution and potentially lower the sample tilt currently required. AES does have the risk of raster burning the surface, especially under high magnification and higher beam currents and voltages. Raster burning can be minimized by beginning with clean samples–solvent cleaning and subsequent heating of the sample in order to desorb some adsorbates from the surface. However, solvent cleaning to remove raster burning after its appearance has not been successful. It is not known whether raster burning would have a negative effect on nonlinear optical properties, such as in a surface waveguide. Prolonged beam exposure is unlikely to change the domain walls (i.e., electron beam poling) with the 5 kV used in this work, but has the potential to do so at higher primary electron beam voltages of approximately 15 kV to 25 kV [33,34]. We have found that 5 kV allows consistent successful

Optical Materials EXPRESS

imaging. A lower bound on the primary beam voltage for AES mapping was not explored, but is likely similar to SEM imaging, where we found that SEM images cannot generally be obtained of the ferroelectric surfaces below primary beam voltages of 1 kV, though this is sample dependent. There are some anomalous horizontal amplitude variations in some maps such as in Fig. 1(a). Their origin is unknown however, on consecutive scans the lines either disappear or shift, suggesting they are random error. They are removed by normalizing each pixel row to the average row value. However, this technique is only valid for images with roughly equal portions of +/-Z domains across the image. Smoothing the AES maps necessarily lowers the spatial resolution but is necessary to remove the pixel-to-pixel noise in order to precisely determine DW locations.

The origin of +/-Z domains' separation in the amplitude of the O-KLL peak signal is currently unknown. Generally, the AES signal is comprised of back-scattered primary electrons, secondary electrons, inelastically scattered Auger electrons from higher energy Auger peaks, and finally the zero loss Auger electrons [35]. It is then necessary to ask whether the peak amplitude separation between +/-Z domains is due to discrepancies in one of these constituents of the Auger signal. +/-Z domains are not separable in the Auger spectra above the Auger O-KLL transition peak (and away from other elemental peaks) however, so it seems that the amplitude contrast is due specifically to the Auger electrons. Perhaps the different surface terminations of +/-Z domains, or different adsorbents on the surfaces [36] are more or less oxygen rich and facilitate the separation in O-KLL amplitude.

5. Conclusion

AES mapping has been demonstrated as a new characterization technique for +/-Z ferroelectric domains in lithium niobate. Mapping unambiguously determines domain orientation relative to each other. AES is generally non-destructive, though further research into whether the beam affects the crystal are needed. AES mapping of domains was compared to the domains after selective HF etching, and are in general agreement. Finally, AES mapping's spatial resolution was demonstrated down to 68 nm, with further improvements possible. This new technique will complement the ambiguous domains, limited spatial resolution, and destructiveness of other established techniques in furthering research on the fabrication of PPLN and other structured poled LN devices.

Funding. National Science Foundation (1710128).

Acknowledgments. The authors gratefully acknowledge G&H for supplying the crystals. This work was performed in part at the Montana Nanotechnology Facility (MONT), a member of the National Nanotechnology Coordinated Infrastructure (NNCI), which is supported by the National Science Foundation under grant number ECCS-1542210. This material is based upon work supported by the National Science Foundation under grant number 1710128.

Disclosures. The authors declare no conflicts of interest.

Data availability. Data underlying the results presented in this paper may be obtained from the authors upon reasonable request.

References

1. E. Soergel, "Piezoresponse force microscopy (PFM)," J. Phys. D: Appl. Phys. **44**(46), 464003 (2011).
2. K. A. Hunnestad, E. D. Roede, A. T. J. van Helvoort, and D. Meier, "Characterization of ferroelectric domain walls by scanning electron microscopy," J. Appl. Phys. **128**(19), 191102 (2020).
3. S. V. Kalinin and D. A. Bonnell, "Local potential and polarization screening on ferroelectric surfaces," Phys. Rev. B **63**(12), 125411 (2001).
4. S. V. Kalinin and D. A. Bonnell, "Imaging mechanism of piezoresponse force microscopy of ferroelectric surfaces," Phys. Rev. B **65**(12), 125408 (2002).
5. G. Rosenman, A. Skliar, I. Lareah, N. Angert, M. Tseitlin, and M. Roth, "Observation of ferroelectric domain structures by secondary-electron microscopy in as-grown $KTiOP_4$ crystals," Phys. Rev. B **54**(9), 6222–6226 (1996).
6. R. L. Bihan, "Study of ferroelectric and ferroelastic domain structures by scanning electron microscopy," Ferroelectrics **97**(1), 19–46 (1989).

Optical Materials EXPRESS

7. V. Aristov, L. Kokhanchik, K.-P. Meyer, and H. Blumtritt, "Scanning electron microscopic investigations of peculiarities of the $BaTi_3$ ferroelectric domain contrast," Phys. Stat. Sol. (a) **78**(1), 229–236 (1983).
8. Y. Sheng, A. Best, H.-J. Butt, W. Krolikowski, A. Arie, and K. Koynov, "Three-dimensional ferroelectric domain visualization by Cerenkov-type second harmonic generation," Opt. Express **18**(16), 16539–16545 (2010).
9. F. Laurell, J. Webjorn, G. Arvidsson, and J. Holmberg, "Wet etching of proton-exchanged lithium niobate-a novel processing technique," J. Lightwave Technol. **10**(11), 1606–1609 (1992).
10. V. Y. Shur, A. I. Lobov, A. G. Shur, S. Kurimura, Y. Nomura, K. Terabe, X. Y. Liu, and K. Kitamura, "Rearrangement of ferroelectric domain structure induced by chemical etching," Appl. Phys. Lett. **87**(2), 022905 (2005).
11. T. Kämpfe, P. Reichenbach, M. Schröder, A. Haußmann, L. Eng, T. Woike, and E. Soergel, "Optical three-dimensional profiling of charged domain walls in ferroelectrics by Cherenkov second-harmonic generation," Phys. Rev. B **89**(3), 035314 (2014).
12. J. Scott, S. Mailis, C. Sones, and R. Eason, "A Raman study of single-crystal congruent lithium niobate following electric-field repoling," Appl. Phys. A **79**(3), 691–696 (2004).
13. A. Gruverman, O. Auciello, R. Ramesh, and H. Tokumoto, "Scanning force microscopy of domain structure in ferroelectric thin films: imaging and control," Nanotechnology **8**(3A), A38–A43 (1997).
14. L. Tian, A. Vasudevarao, A. N. Morozovska, E. A. Eliseev, S. V. Kalinin, and V. Gopalan, "Nanoscale polarization profile across a 180° ferroelectric domain wall extracted by quantitative piezoelectric force microscopy," J. Appl. Phys. **104**(7), 074110 (2008).
15. S. Zhu and W. Cao, "Imaging of 180° Ferroelectric Domains in $LiTaO_3$ by Means of Scanning Electron Microscopy," Phys. Stat. Sol. (a) **173**(2), 495–502 (1999).
16. S. Zhu and W. Cao, "Direct Observation of Ferroelectric Domains in $LiTaO_3$ Using Environmental Scanning Electron Microscopy," Phys. Rev. Lett. **79**(13), 2558–2561 (1997).
17. W. Cao and S. Zhu, "Observation of ferroelectric domains in $LiTaO_3$," Ferroelectrics **226**(1), 27–35 (1999).
18. T. McLoughlin, W. R. Babbitt, and W. Nakagawa, "Nano-scale ferroelectric domain differentiation in periodically poled lithium niobate with auger electron spectroscopy," Opt. Continuum **1**(4), 649–659 (2022).
19. D. R. Baer, A. S. Lea, J. D. Geller, J. S. Hammond, L. Kover, C. J. Powell, M. P. Seah, M. Suzuki, J. F. Watts, and J. Wolstenholme, "Approaches to analyzing insulators with Auger electron spectroscopy: Update and overview," J. Electron Spectrosc. Relat. Phenom. **176**(1-3), 80–94 (2010).
20. K. Tsutsumi, T. Suzuki, and Y. Nagasawa, "Effective methods to prevent charging in auger electron spectroscopy," JEOL News **36E**, 66–70 (2001).
21. Y. Yun, M. Li, D. Liao, L. Kampschulte, and E. I. Altman, "Geometric and electronic structure of positively and negatively poled $LiNbO_3$ (0001) surfaces," Surf. Sci. **601**(19), 4636–4647 (2007).
22. T. McLoughlin, W. R. Babbitt, P. A. Himmer, and W. Nakagawa, "Auger electron spectroscopy for surface ferroelectric domain differentiation in selectively poled MgO:$LiNbO_3$," Opt. Mater. Express **10**(10), 2379–2393 (2020).
23. Y. Zhou, D. S. Fox, P. Maguire, R. O'Connell, R. Masters, C. Rodenburg, H. Wu, M. Dapor, Y. Chen, and H. Zhang, "Quantitative secondary electron imaging for work function extraction at atomic level and layer identification of graphene," Sci. Rep. **6**(1), 1–8 (2016).
24. W. L. Holstein, "Etching study of ferroelectric microdomains in $LiNbO_3$ and MgO:$LiNbO_3$," J. Cryst. Growth **171**(3-4), 477–484 (1997).
25. C. L. Sones, S. Mailis, W. S. Brocklesby, R. W. Eason, and J. R. Owen, "Differential etch rates in z-cut $LiNbO_3$ for variable HF/HNO_3 concentrations," J. Mater. Chem. **12**(2), 295–298 (2002).
26. P. R. Potnis, N.-T. Tsou, and J. E. Huber, "A review of domain modelling and domain imaging techniques in ferroelectric crystals," Materials **4**(2), 417–447 (2011).
27. S. Mailis, C. L. Sones, J. G. Scott, and R. W. Eason, "UV laser-induced ordered surface nanostructures in congruent lithium niobate single crystals," Appl. Surf. Sci. **247**(1-4), 497–503 (2005).
28. V. Bermúdez, F. Caccavale, C. Sada, F. Segato, and E. Diéguez, "Etching effect on periodic domain structures of lithium niobate crystals," J. Cryst. Growth **191**(3), 589–593 (1998).
29. C. Y. J. Ying, C. L. Sones, A. C. Peacock, F. Johann, E. Soergel, R. W. Eason, M. N. Zervas, and S. Mailis, "Ultra-smooth lithium niobate photonic micro-structures by surface tension reshaping," Opt. Express **18**(11), 11508–11513 (2010).
30. K. Nassau, H. J. Levinstein, and G. M. Loiacono, "The domain structure and etching of ferroelectric lithium niobate," Appl. Phys. Lett. **6**(11), 228–229 (1965).
31. S. Kim, V. Gopalan, and A. Gruverman, "Coercive fields in ferroelectrics: A case study in lithium niobate and lithium tantalate," Appl. Phys. Lett. **80**(15), 2740–2742 (2002).
32. C.-L. Jia, S.-B. Mi, K. Urban, I. Vrejoiu, M. Alexe, and D. Hesse, "Atomic-scale study of electric dipoles near charged and uncharged domain walls in ferroelectric films," Nat. Mater. **7**(1), 57–61 (2008).
33. Y. Glickman, E. Winebrand, A. Arie, and G. Rosenman, "Electron-beam-induced domain poling in $LiNbO_3$ for two-dimensional nonlinear frequency conversion," Appl. Phys. Lett. **88**(1), 011103 (2006).
34. C. Restoin, C. Darraud-Taupiac, J.-L. Decossas, J.-C. Vareille, V. Couderc, A. Barthélémy, A. Martinez, and J. Hauden, "Electron-beam poling on Ti:$LiNbO_3$," Appl. Opt. **40**(33), 6056–6061 (2001).
35. H. Bishop, "The Role of the Background in Auger Electron Spectroscopy," Scanning Electron Microscopy, Volume 1982(1), 22 (1982).

Optical Materials EXPRESS

36. S. Sanna and W. G. Schmidt, "$LiNbO_3$ surfaces from a microscopic perspective," J. Phys.: Condens. Matter **29**(41), 413001 (2017).